Experimental and Time-Dependent Density Functional Theory Modeling Studies on the Optical Properties of Carbon Nanodots

By: Alex T. Sheardy, Durga M. Arvapalli, and Jianjun Wei

A. T. Sheardy, D. M. Arvapalli, J. Wei, Experimental and Time-Dependent Density Functional Theory Modeling Studies on the Optical Properties of Carbon Nanodots. *Journal of Physical Chemistry C* **2020**, 124, 8, 4684-4692. DOI: 10.1021/acs.jpcc.9b10373.

Abstract:

Carbon nanodots (CNDs) are zero-dimensional carbon particles that have attracted interest in a variety of applications mostly because of their small size, structure–function versatility, and photoluminescence properties. Unfortunately, the complicated and varied structures of particles that fall under the umbrella of "CNDs" make prediction of the optical properties difficult to determine empirically. It is thus far more practical to use computational methods, such as density functional theory (DFT), to predict the optical properties of different potential structures. Herein, two different syntheses of CNDs with noticeably different optical properties are presented for demonstration. Time-dependent DFT on twelve different proposed structures was then performed in order to elucidate the nature of the absorptive properties. The main result of these calculations is that deformations in the graphitic structure of CNDs seem to dominate the effects on the optical transitions, particularly the π–π* transitions, in comparison with experimental results.

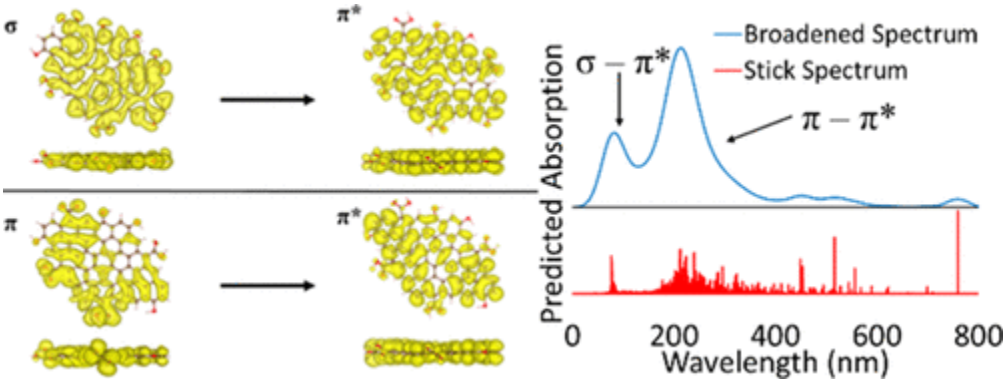

Keywords: Carbon nanodots (CNDs) | density functional theory (DFT) | time-dependent DFT (TDDFT)

Article:

Introduction

First discovered by accident in 2004 by Xu et al.,[1] carbon dots (CDs) have been a focus of research for a wide variety of applications, including bioimaging and theranostics,[2−6] drug delivery,[7−9] antioxidation,[10−12] and use in solar cells.[13,14] Depending on the desired application, a wide variety of synthetic approaches can be used, and these varied methods result in varied structures and properties.[15−17] This is because, unlike traditional metallic and inorganic semiconducting nanoparticles which possess well-defined crystalline structures, the true structure of CDs is nonobvious. In fact, based on the report of Zhu et al.,[18] "CDs" can be further divided into three subgroups; graphene quantum dots (GQDs), carbon nanodots (CNDs), and polymer dots (PDs). These particles are listed in the order of increasing sp^3 character, with GQDs being almost entirely graphitic, CNDs possessing a mixture of graphitic and diamond-like character, and PDs containing small sp^2 domains linked by larger polymer (sp^3) chains. The mixture of graphitic and diamond-like structures in CNDs leads to their unique optical properties but also makes prediction of these properties an interesting challenge.

The major defining differences between synthetic methods are the carbon sources being used to produce the CNDs. Generally, there are two routes that can be used to produce CNDs: top-down and bottom-up approaches. Top-down methods start with large carbonaceous materials (graphite, carbon nanotubes, etc.), which are then broken down into smaller particles. Because the source materials start with graphitic structures, the produced CNDs maintain this hybridization but often need postsynthetic modification and/or doping to achieve photoluminescence (PL).[18−20] Bottom-up methods start with smaller molecules such as carbohydrates,[3,5,14] alcohols,[21] and citric acid,[22−25] among others,[7,26,27] which are reacted to form larger particles. The increased variety of starting materials results in highly diverse structures and compositions. In addition to carbon, most CNDs contain oxygen, while others may also incorporate nitrogen,[22,28] sulfur,[12,29,30] and/or phosphorous.[31] The different structures and compositions can lead to different properties and potential applications.

One of the main advantages of CNDs over other materials is that the synthesis can often be performed in a way that allows for ideal properties for a given application. For example, our group has shown that both carboxylic acids and amines can contribute to the antioxidative properties of CNDs,[10] and these properties can be further enhanced by the addition of sulfur.[12] CNDs can also exhibit excitation-dependent fluorescence, which can be helpful for bioimaging or solar conversion applications.[14,18,28] Alternatively, some groups have synthesized CDs that do not show excitation-dependent fluorescence.[5,29] The specific energy and quantum yield are dependent on the surface functionality,[18] though reports are often conflicting in the exact way the functionality affects the photophysics.

The complicated and diverse nature of CND structures makes an empirical synthetic study on the nature of the optical properties of CNDs a futile effort. For example, simply changing a single precursor molecule to change the functional groups may also result in changes to the structure in ways that cannot be predicted. The addition of the functional group may result in changes to either surface functionality and/or the graphitic structure, both of which can change the optical properties. There have been some attempts to study the optical properties of CNDs computationally, but these efforts have been focused on the specific particles synthesized in the earlier mentioned studies. Specifically, Strauss et al. studied the optical absorption/emission properties of six possible CND structures with density functional theory (DFT); and all of the

studied structures contain both oxygen and nitrogen atoms.[25] Similarly, the GQDs studied with DFT reported by Jin et al. contain nitrogen but no oxygen.[32] Li et al. used DFT to explore the structure of some oxygen- and/or sulfur-doped CNDs but did not study the optical properties of these particles.[30] As such, there remains a lack of understanding on the relationship between the structure and optical properties of CNDs. Herein, we present two examples of syntheses to showcase the different optical and structural properties that can be observed in CNDs. Further, we used time-dependent DFT (TDDFT) to predict the optical absorption of twelve possible CND structures and attempt to correlate the observed optical properties with the structure of the particles.

Experimental Section

Synthesis of CNDs. Two different syntheses were used to produce CNDs with different properties. The first synthesis was based on the procedure reported by Hu et al.[22] Specifically, this synthesis involved combining 960 mg of citric acid (Acros Organics) and 1 mL of ethylene diamine (Fisher Scientific) in 1 mL of deionized (DI) H_2O. This mixture was then heated in a microwave synthesizer (CEM Discover) at 300 W for 18 min. The resulting solid was then dissolved in 5 mL of DI H_2O, resulting in a dark red-brown solution. Throughout the rest of the article, these particles will be referred to as E-CNDs. Alternatively, a variation of the synthesis reported by Bhunia et al.[3] was used. In this procedure, 1.5 g of sucrose (Sigma-Aldrich) was first dissolved in 5 mL of DI H_2O, and the solution was placed in an ice bath. To this solution, 5 mL of conc. hydrochloric acid (12.1 M, Acros Organics) was slowly added (dropwise) to minimize heating. The mixture was heated at 90 °C for 25 min and then cooled and placed in an ice bath. To neutralize the HCl, ~3.2 mL of NaOH (18.94 M, Fisher Scientific) was slowly added, again minimizing heating. These particles will be referred to as suc-CNDs throughout the remainder of the article. Following either synthesis, the particles were purified by dialysis (1000 MWCO) and dried by freeze-drying to obtain solid products.

Characterization of CNDs. A number of different characterization techniques were used to determine the structure and properties of the synthesized CNDs. The size of the particles was determined using atomic force microscopy (AFM) because the small size and low contrast makes TEM difficult to obtain. For the AFM, a solution of the particles was drop-cast onto a freshly cleaved mica surface. Because of equipment failure, the suc-CNDs were measured on an Agilent 5600LS AFM, while the E-CNDs were measured with an Asylum MFP-3D Origin+ AFM, but each image was acquired using similar parameters and probes. UV–vis (Varian Cary 6000i) and fluorescence (Horiba FluoroMax-4) spectroscopies were used to measure the optical properties of the materials. Fourier transform infrared (FTIR), ^{1}H NMR, and ^{13}C NMR (Agilent) were performed on the CNDs to determine the functional groups present on these materials. NMR spectra were obtained by dissolving the samples in D_2O and were averaged over 32 (^{1}H) or 10,000 (^{13}C) scans. X-ray photoelectron spectroscopy (XPS) (Thermo ESCALAB Xi^{+}) was performed to analyze the elemental composition of each sample. X-ray diffraction (XRD) (Agilent) and Raman (Horiba Raman confocal microscope) were performed to provide insights into the structure of both particles.

DFT Modeling of CNDs. To model the optical properties of different CND structures, TDDFT calculations were carried out on multiple structures using ABINIT.[33−37] The structures were

made up of a pure graphitic sheet ($C_{70}H_{22}$), to which different functionalities including hydroxides, carboxylic acids, epoxides, and amines were added but on the exterior of the sheet and as internal defects. To treat each molecule as isolated, the structures were placed in a 60 × 60 × 25 bohr box. The calculations were performed by first relaxing structures using a tolerance on the difference of force of 5×10^{-6} hartree/bohr, with a maximal force of 5×10^{-5} hartree/bohr. Following this is an additional energy relaxation with an energy difference cutoff of 1×10^{-7} hartree. Finally, the TDDFT calculation is performed using a tolerance on a wave function squared residual of 10^{-9}. For the TDDFT to be performed, only a single *k*-point at Γ (0, 0, 0) can be used. These experiments result in relaxed structures of the molecules, the energy eigenstates, and the transition probabilities between eigenstates.

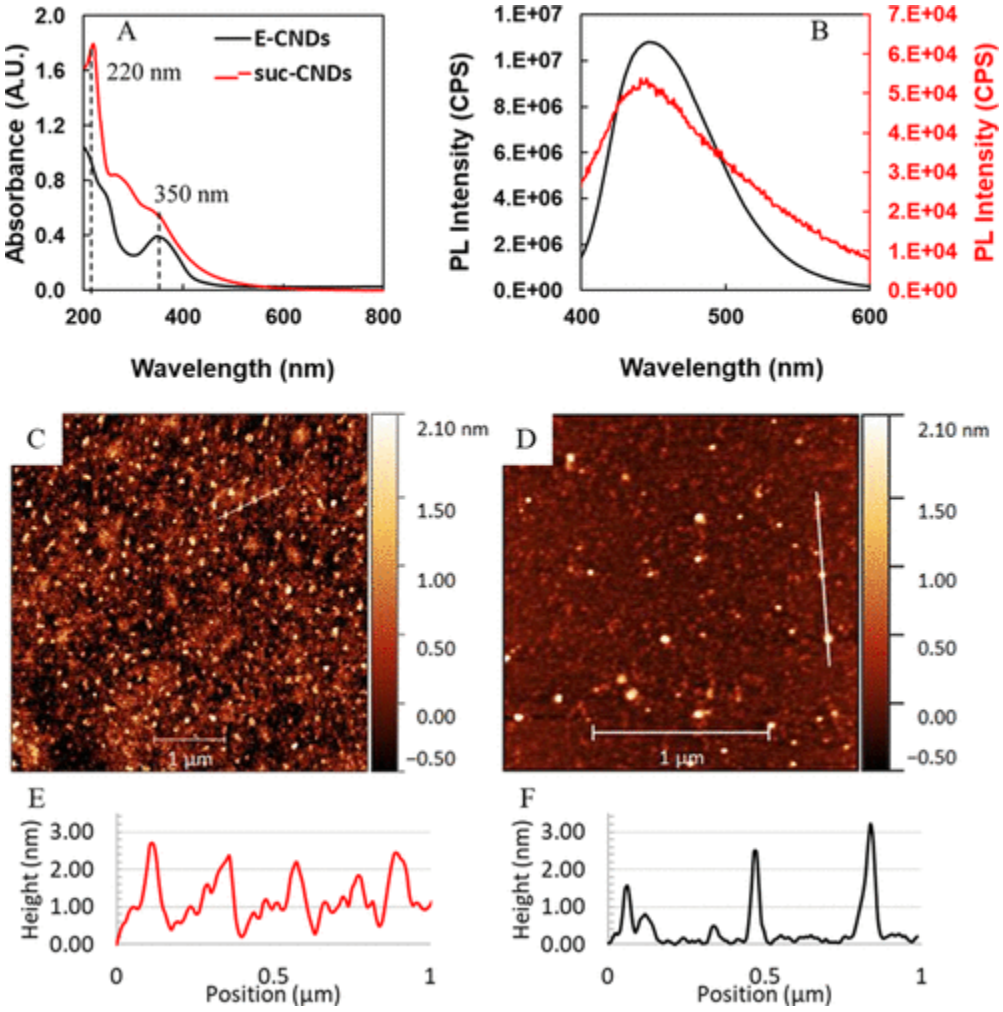

Figure 1. UV–vis (A) and PL (B) spectroscopies of both E-CNDs (black) and suc-CNDs (red). PL data needed to be plotted on separate *y*-axes because of large differences in the magnitude of the PL signal. For the UV–vis, both samples were at a concentration of 0.1 mg/mL, while for the PL measurements, the concentrations were 0.05 mg/mL. AFM of suc-CNDs (C), E-CNDs (D), and associated height profiles along the lines are shown on the AFM image (E,F, respectively). The scale bar on each AFM image is 1 µm.

Results and Discussion

CNDS were successfully synthesized using the above described methods. UV–vis and PL emission spectroscopies were performed for both samples (Figure 1). In the UV–vis spectrum, both samples exhibit high intensity absorption at around 220 nm, which gradually decreases at higher wavelengths. However, the shape of these decreases is noticeably different between the two different synthetic methods. After the strong peak at 200 nm, the E-CNDs have a small shoulder at around 230 nm and then the absorbance rapidly drops until there is a strong peak at 350 nm. For these particles, no significant absorbance is observed above ∼400 nm. The suc-CNDS on the other hand have a much slower decrease, with two shoulders at 285 and 350 nm, and continue to have a decaying absorbance up to ∼600 nm. For the PL studies, the E-CNDs exhibited a strong signal at 450 nm, while the suc-CNDs had a much weaker emission at 445 nm.

AFM was performed to determine the size of the particles, specifically by using the height of the particles because the resolution in the *XY* plane is limited by the AFM probe (Figure 1C,D). From the AFM height profiles (Figure 1E,F), both synthetic methods result in sizes on the order of 1.5–3 nm. The average sizes for the particles are 1.4 and 2.1 nm for the suc-CNDs and E-CNDs, respectively, and size distributions can be found in Figure S1. FTIR spectroscopy was performed on each type of CND, which reveals the presence of different functional groups (Figure S2). Specifically, both structures have O–H and C–H stretches at 3300 and 2920 cm^{-1}, respectively. However, the area around the O–H stretch on the E-CNDs possesses additional features, likely from N–H stretches. Additionally, while each spectrum presents peaks at ∼1635 cm^{-1} for C═O stretches, this peak is significantly more intense in the E-CNDs. The E-CNDs also feature a prominent peak at 1535 cm^{-1}, which can be attributed to the N–H bend. Both structures have peaks in the 1300–1400 cm^{-1} region arising from C═C stretches. Finally, the suc-CNDs have a medium strength peak at 1025 cm^{-1}, which can arise from the C–O stretching.

Both ^{1}H and ^{13}C NMR were performed on the two samples to further analyze the potential functional groups (Figure S3). The complex nature of CND structure makes exact interpretation of the NMR difficult, but specific functional groups can be identified based on peak shifts. For both samples and both ^{1}H and ^{13}C NMR, there are clearly aliphatic and hydroxyl hydrogens/carbons. Additionally, there are ^{13}C peaks in the 150–180 ppm region, indicating C═O and/or C═C. However, only the suc-CNDs have a strong ^{1}H signal in this region, indicating that the C═O can only be either a carboxylic acid or ketone and that the outside of the graphitic structure is likely functionalized with heteroatoms (i.e., OH groups). The ^{1}H signal at 8.3 ppm is likely due to aromatic hydrogens, so the surface of these CNDs is not entirely functionalized. While no carboxylic acid hydrogens are observed, this may easily be attributed to proton/deuterium exchange with the solvent (D_2O). Finally, the ^{1}H NMR for the E-CNDs shows a peak at ∼2.8 ppm and several peaks at 5.8 ppm, which can be correlated with amines and amides, respectively. Summarizing the results of both FTIR and NMR, both structures have characteristics of graphitic cores covered with oxygenaceous functional groups (hydroxyls and carboxylic acids), while the E-CNDs also have nitrogenous groups (amines and amides).

In order to determine the elemental composition of each sample, XPS was performed (Figure S4A). The suc-CNDs were found to contain 62% carbon and 38% oxygen, while the E-CNDs contained 57% carbon, 22% nitrogen, and 20% oxygen. To determine if the CNDs possess a graphitic or amorphous structure, XRD (Figure S4B) and Raman (Figure S4C) were also

performed. Both CNDs present peaks corresponding to the (002) index;[38] however, these peaks do occur at different angles. Specifically, the suc-CND peak is centered at ∼17.8° (fwhm = 13°), corresponding to a lattice spacing of 0.47 Å, while the E-CND peak is centered at 23.2° (fwhm = 12.6°), corresponding to a lattice spacing of 0.39 Å. Finally, in the Raman spectra for these samples, both D and G peaks can be seen, with D/G ratios of 1.15 and 1.29 for suc-CND and E-CNDs, respectively. The broadness of both the XRD and Raman peaks indicates that the particles are amorphous; however, the presence of the (002) peak shows that there is a graphitic character in both of these particles.[11,15,39] Further, the different angles for the (002) peak suggest that the functionalization of the graphitic structure is different between the particles. Specifically, the larger lattice spacing of the suc-CNDs, combined with the higher oxygen content, suggests a larger degree of internal oxygen functionalization on the graphitic structure than the E-CNDs. However, the smaller D/G ratio for the suc-CNDs shows that there may be larger amorphous regions within the structure of the E-CNDs. One possible explanation for these combined results is that the suc-CNDs include a structure, resembling layers of graphene oxide within the amorphous bulk, while the E-CNDs have less oxidized graphitic regions surrounded by amorphous/polymeric regions. Additionally, the size of the graphitic lattice is expected to largely determine the wavelength of the fluorescence emission,[40,41] and because both particles have similar emission wavelengths, similar sized graphitic structures are expected for both CNDs.

The differences between these particles, particularly in regard to the PL emission intensity and the strong absorption peak at 350 nm, led to a question: what is responsible for these differences? At quick inspection, the most obvious differences between these syntheses are the presence of nitrogenous functional groups in the E-CNDs and the increased degree of internal graphitic functionalization in the suc-CNDs. While a comprehensive synthetic study using varying elemental compositions would be possible, the complex structural nature of CNDs makes this approach incomplete. Instead, it is far more reasonable to compare theoretical spectra from a number of different potential CND structures (**I–XII** in Figure S5). The first structure calculated was a simple graphitic sheet (**I**) with no functional groups. This structure is likely not very representative of the materials synthesized but does provide a baseline for looking at the effects of functional groups on the absorptive properties. All other structures were based on this sheet, starting with the addition of both hydroxides and carboxylic acids (**II**), which are present on all following structures. From here, multiple internal defects/functional groups were added, including a 5-7-7-5 Stone–Wales defect (**III**), hydroxides (**IV**), epoxides (**V**), and a combination of hydroxides and an epoxide (**VI**). The remaining structures started to incorporate nitrogen both as surface and internal functional groups. Specifically, first, only external primary amines were added (**VII**), followed by the groups with internal secondary amines disrupting the graphitic lattice (**VIII**) and a combination of structures **VI** and **VIII** having internal oxygens and nitrogens (**IX**). Finally, a series of structures containing 2, 4, or 6 internal tertiary amines were studied (**X**, **XI**, and **XII**, respectively). All structures have an approximate length of 1.2 nm along both the zigzag and armchair sides prior to relaxation, which is on the lower end of the size scale for CNDs. However, increasing the number of atoms greatly increases the computational time and resources required for these calculations. This is also the reason that only a single sheet was modeled for each structure. While the studied structures do not represent the complete amorphous structure of the CNDs, the sp^2 regions largely determine the optical properties of these materials,[40,41] and this sized graphitic region is expected to approximate the observed experimental fluorescence.[32,42]

Using DFT, optimized geometries for each of the above structures were generated (Figure 2). As could be expected, structures with only external functional groups (**I**–**II** and **VII**) and structures that have tertiary nitrogens within the graphitic lattice (**X**–**XII**) are still fairly planar. However, the remaining structures with disruptive internal functional groups do show significant deviations for a planar graphene sheet. To analyze these disruptions, the positions of the carbon atoms in the relaxed structures were extracted and fit to a plane using MatLab, and the root mean square (RMS) error of this fit is an estimate of planarity (Table 1, Figure S6). This value will be used in the spectral analysis.

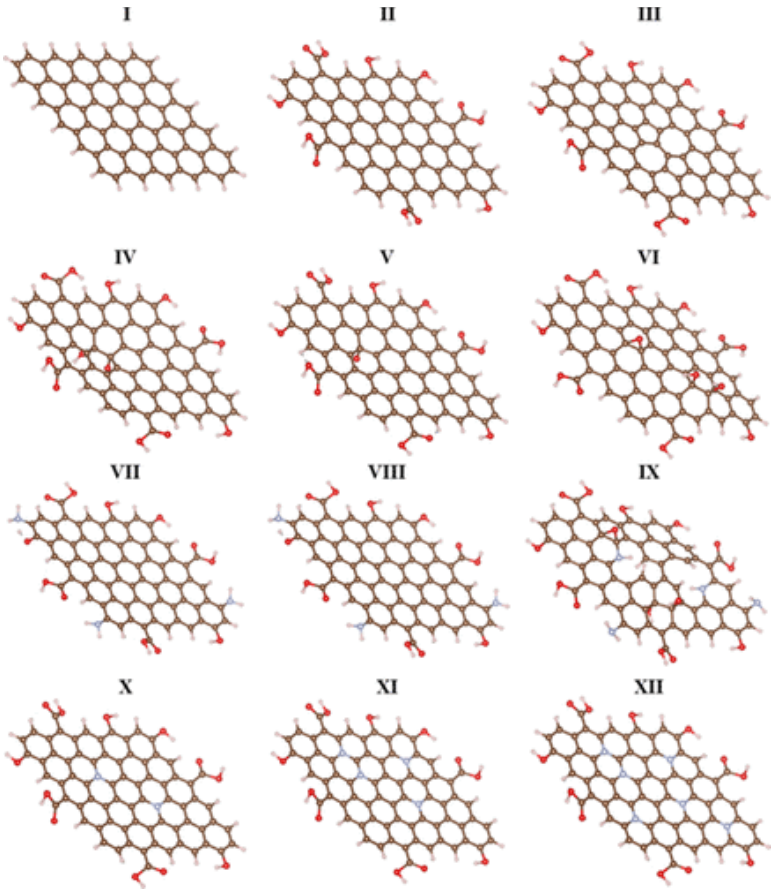

Figure 2. DFT-optimized geometries for structures **I–XII**. Dark gray atoms are carbon, light gray atoms are hydrogen, red atoms are oxygen, and blue atoms are nitrogen.

Following the structural relaxation, TDDFT calculations were performed to examine the electronic spectra of the tested structures. These calculations result in the energies and probabilities for the transitions from the occupied to unoccupied states. Further analysis of the results was also performed using several different approaches. First, to generate realistic looking electronic spectra, each of the transitions was broadened into a gaussian function with a full width at half-maximum (fwhm) of 2.5 nm, and all the gaussian functions were added together (Figure 3A). A representative final spectrum and a stick spectrum showing the original data is found in Figure 3B, and the remaining spectra can be found in Figure S7. Second, the number of allowed transitions (oscillator strength > 10^{-6}) was compared to number of possible transitions to get a percentage of allowed transitions. Finally, the summed intensity of the major π–π*

transitions and the percent of allowed transitions were compared against the RMS error of the planar fitting (Figure 3C). The data from these results are in summarized in Table 1.

Table 1. Summary of Results from Calculations for Structures I–XII[a]

structure	RMS	peak height	allowed transitions	possible transitions	% allowed transitions (%)
I	0.006	7.599	364	1812	20.1
II	0.079	6.112	1370	2730	50.2
III	0.129	5.323	1442	2730	52.8
IV	0.257	4.498	1795	2828	63.5
V	0.154	4.941	1605	2772	57.9
VI	0.298	4.288	2042	3075	66.4
VII	0.072	5.894	1576	3060	51.5
VIII	0.279	4.630	1910	3015	63.3
IX	0.341	3.604	2332	3376	69.1
X	0.073	4.997	1501	2772	54.1
XI	0.071	3.793	1741	2758	63.1
XII	0.067	5.571	1450	2744	52.8

[a] Included is the RMS error of the fitting of carbon atoms to a plane, height of the π–π* transition, the number of allowed and possible transitions, and the percent of allowed transitions.

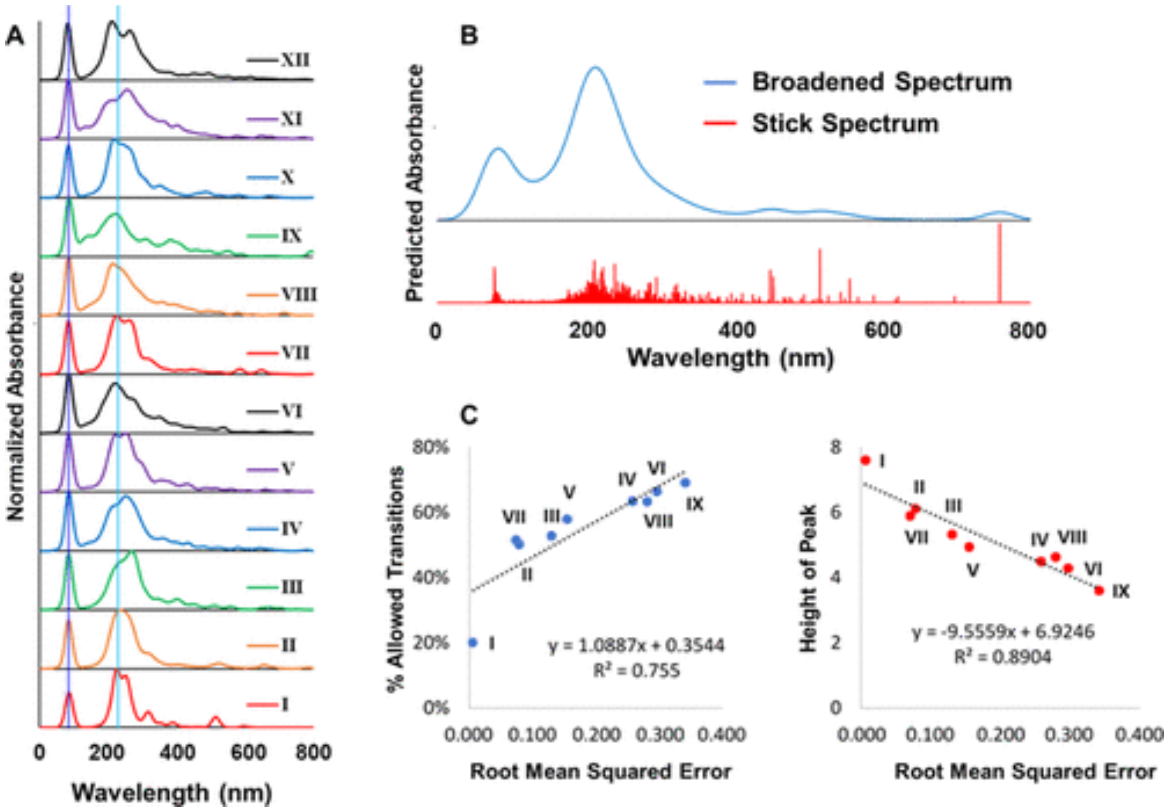

Figure 3. (A) Predicted UV–vis absorption spectra for structures **I**–**XII**. These spectra have been normalized to the most intense peak and offset for clarity. (B) Representative Gaussian broadened (blue) and stick (red) spectra from structure **II**. (C) Plots of the percent of allowed transitions (left, blue dots) and the height of the π–π* transition (right, red dots) vs the RMS error of the fitting of the optimized structure to a plane. The dotted line represents a linear fit of the data, and the equation and R^2 of the fit are given.

Looking at the produced spectra, there are clearly two major peaks/sets of peaks at ~90 nm and between 150 and 400 nm present for all molecules. For clarity, the presented spectra have been normalized by the intensity of the strongest peak, but any following arguments referring to peak intensity are based on the un-normalized data. From the data, the peak at 90 nm is a σ–π* transition and does not seem to vary significantly in terms of position, width, or intensity between the different structures. Additionally, this peak is at too high energy to be detected using a standard UV–vis spectrometer and is therefore not present in the experimental spectra. The peak(s) at around 150–400 nm result from π–π* transitions and do vary greatly in position, width, intensity, and number. Representative wave functions showing these transitions in the structure **II** can be found in Figure 4. Before discussing specifics relating to functional groups, some of the observed bulk trends shall be discussed. For structures **I–IX** (**X–XII** do not follow these trends and will be discussed later), two general trends were observed regarding the planarity of the molecule (RMS error) and the number of allowed transitions or the intensity of the π–π* transition. Specifically, the number of allowed transitions increases roughly linearly ($R^2 = 0.76$) with the RMS error, although this trend shows higher linearity ($R^2 = 0.97$) even if the pure graphitic structure (**I**) is not included. Conversely, the intensity of the π–π* transition decreases linearly ($R^2 = 0.89$) with increasing RMS error.

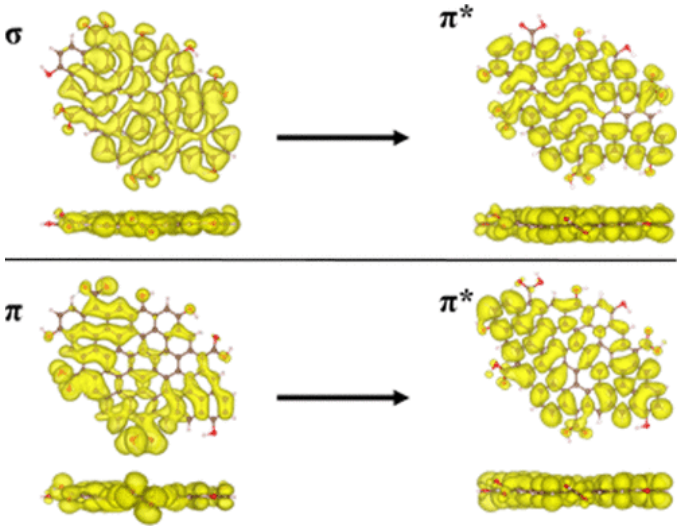

Figure 4. Representative σ–π* transition (top) and π–π* transition (bottom) for the structure **II**. Yellow represents the wave function.

Taken together, the abovementioned trends suggest the following behavior: as structural distortions increase, the strength of individual transitions decreases, while new transitions become allowed. For the graphitic structure (**I**), the ideal planar structure results only in transitions between specific states with a high degree of wave function overlap. As new functional groups are added, the structure distorts and the overlap of these wave functions decreases. However, these structural distortions also result in overlap between states that previously did not overlap. The newly introduced transitions will also fall at slightly different energies than the previous transitions, introducing more width to the peak. While the introduction of functional groups also adds new types of states, the significant increase in the percent of allowed transitions suggests that this trend is due to the change in the graphitic

structure rather than any new functional group-dependent transitions. Further, while the small deviations from linearity are likely due to the specific functional groups, this data does suggest that the most important factor in determining the optical properties of CNDs is the number of disruptive functional groups, rather than the specific elements present. Finally, the experimental spectra show a peak/shoulder at 350 nm, which is generally attributed to n−π* transitions but is not observed in the predicted spectra.[43] An explanation for this is that the functional groups leading to the n−π* transition must be resonance-isolated from the main graphitic structure which has too many π* states to result in a single peak.

The major exceptions to this rule are the structures that contain internal tertiary amines (**X–XII**), the spectra for which are shown in Figure 5, along with the nitrogen-less analogue (**II**). From Table S1, there is a slightly decreasing trend in the planarity of these structures, but the spectra show more significant differences than the previous discussion would predict. It can be seen that there is a single major peak at around 250 nm in the absence of nitrogen, but as nitrogens are introduced, the peak weakens and separates into multiple peaks/shoulders. Increasing from zero to four nitrogens, the peak consistently lowers in intensity and broadens; however, the structure with six nitrogens appears between the two and four nitrogen structures. This suggests that as nitrogen defects in the graphitic lattice are added, the overlap between transitions also improves, potentially due to the lone pair of electrons in the p-orbital of the nitrogen. Further, these trends might help explain the difference in the observed experimental spectra, but more data would be needed to confirm this hypothesis.

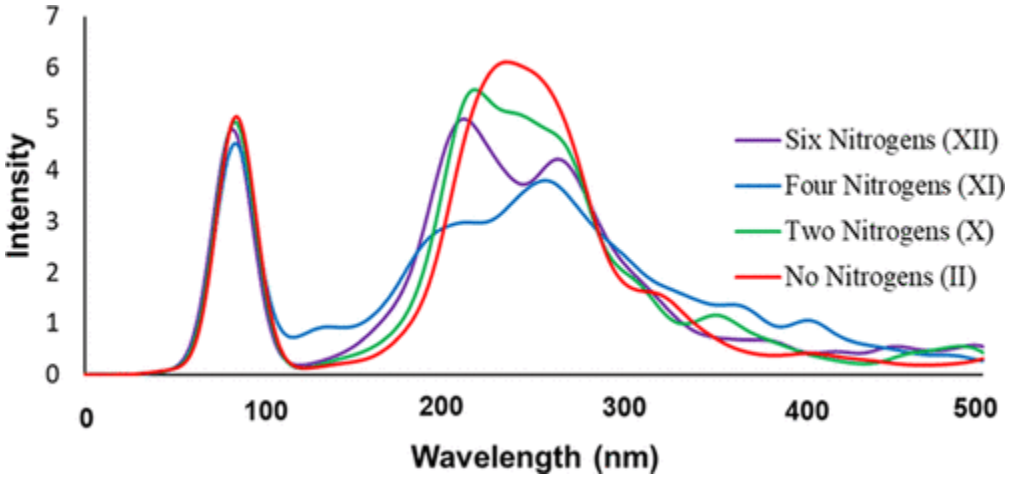

Figure 5. Predicted UV–vis absorption spectra for structures **II** and **X–XII**, structures where carbon atoms in the graphitic structure have been replaced by 0, 2, 4, or 6 nitrogen atoms.

The combination of these experimental and computational results along with an observation by Fu et al. might help in explaining the difference in fluorescence intensity between the suc-CNDs and E-CNDs.[44] Specifically, Fu et al. observed that the fluorescence intensity increases with decreasing interlayer distance because of the presence of trap states between graphitic layers. The XRD results for E-CNDs clearly show a decreased interlayer distance of 0.39 versus 0.47 Å for the suc-CNDs. Incorporation of nitrogen atoms within the graphitic lattice does not noticeably disrupt the planarity of the structure, allowing for closely packed layers and higher fluorescence, as seen in the nitrogen-containing E-CNDs. Conversely, high oxygen content can

cause larger disruptions to the planar structure, resulting in larger interlayer distances and weaker fluorescence, as seen in the suc-CNDs.

As previously stated, certain optical properties (overall height of peak and allowed transitions/width) of CNDs seem to be primarily dominated by the distortions within the graphitic structure, regardless of the specific functional groups. Regarding the shape of the π–π* transition peak, nearly all of the studied structures show at least two peaks in this 200–300 nm range, the main exception being structure **II**. However, this peak is still asymmetrical, indicating that it may be composed of multiple groups of transitions. While multiple peaks are present for each structure, the relative intensities and positions of each do change with the functional groups present. For example, structures **IV–VI** (those containing internal alcohols and/or an epoxide) present similar spectra, with two peaks/shoulders at ∼220 and ∼250 nm. The introduction of the hydroxide groups in structures **IV** and **VI** leads to similar structural disruptions and overall peak intensity in both samples, and these groups are more disruptive than only having an epoxide. Adding only surface primary amines (**VII**) has little effect on the optical properties, but internal secondary amines (**VIII–IX**) do introduce significant distortions and the corresponding spectral changes related to these distortions.

An important factor in discussion is the actual electronic structure of the proposed CND structures and how this relates to the generated spectra. For this discussion, the available electronic levels occupying structure **II** and their room temperature are given in Figure 6. These energy levels can give information about the energy of fluorescent photons that can be emitted from the structure, but prediction of fluorescence intensity is dependent on factors such as surface passivation and is therefore harder to predict. As can be seen, the major transitions do not come from highest occupied molecular orbital (HOMO)–lowest unoccupied molecular orbital (LUMO) excitations, as the HOMO–LUMO gap is only 0.16 eV (∼7750 nm). Considering that pure infinite graphene is a zero-band gap semiconductor,[45] it is not surprising that a smaller graphitic sheet has a small band gap. Using this specific structure as an example, the transitions between 195 occupied and 14 unoccupied states were calculated. These states are numbered according to increasing energy (Figure 6), with state 1 being the lowest energy occupied state, state 195 being the HOMO, and state 196 being the LUMO. As previously mentioned, the highest energy transition at 90 nm is a σ–π* transition, specifically with the transition between states 50 and 205 being a major contributor (Figure 4, top). For the π–π* transitions, a higher energy occupied state is excited to a low-lying unoccupied state; for example, the excitation from state 173 to 206 is a significant contribution (Figure 4, bottom). This does suggest that π–π* transitions may be more important than n−π* transitions in determining the optical properties, at least in terms of excitation. The produced electronic structure may also help to explain the excitation-dependent fluorescence observed in some CNDs.[14,18,28] Because there are clearly multiple energy levels that have similar energies, different incident excitation energies can excite either different energy electrons or the same electron to a different energy, resulting in different energy PL. Because the majority of the energy levels are either π or π*, this suggests that excitation-independent fluorescence would likely arise from CNDs with smaller aromatic systems, such that there are fewer possible transitions.

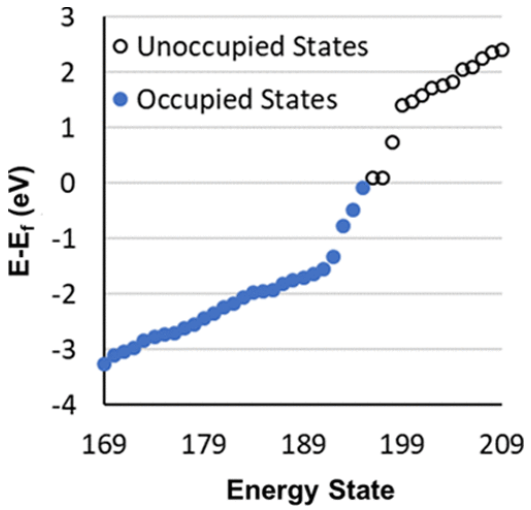

Figure 6. Plot of occupied (blue) and unoccupied (black hollow) states present in the structure **II**. Energy on the *y*-axis is relative to the Fermi energy.

Further, while the introduction of new functional groups is expected to change the electronic structure of these particles,[41,42] this cannot be the sole explanation for the observed changes. Specifically, the two factors that have been correlated with planarity, peak intensity, and % allowed transitions cannot be explained by changes to the electronic structure alone. For example, the only difference between structures **II** and **IV** is the addition of two hydroxyl groups. The structure **II** has 195 occupied states, while **IV** has 202 occupied states, and the same number of unoccupied states (14) was used for both. This is expected, as a single C–C π orbital is removed, while 2 C–O σ bonds, 2 O–H σ bonds, and 4 non-bonding oxygen orbitals are added. Therefore, the changes expected purely from the loss and introduction of new electron states are not expected to have a significant effect on the π–π* absorption. However, the observed result is that the peak absorption intensity decreases from 6.1 to 4.5, while the number of allowed transitions increases by 425, even though only 98 new possible transitions are introduced. The removal of a C–C π orbital can cause further changes to the electronic structure, but the significant changes in the transition probability are attributed to structural deformations and increases/decreases in orbital overlap.

Comparing the experimental results to the computation results, it is clear that there are some discrepancies between the two. However, many of these discrepancies can be explained by one of the fundamental challenges in the study of CNDs, uniformity. While repeated syntheses under identical conditions will yield particles with the same overall properties, the properties of particles from a given synthesis cannot be ascribed to an individual structure. This is the reason that many CNDs exhibit broad peaks in a number of different characterization techniques; for example, Raman, XRD, UV–vis, and PL. One of the inconsistencies between the theory and the experiment is the presence of theoretical absorption peaks at wavelengths longer than ~500 nm, which are not observed in the experimental results. An explanation for this is simply the energy of these transitions varying from structure to structure and a real CND sample being likely a combination of these and/or other structures. Averaging the predicted spectra for some combination of the studied structures would result in minimal absorption at longer wavelengths, as shown in the experimental results. To exactly compare experimental and theoretical studies on CNDs, extraordinary purification and characterization techniques would be required to ascertain

the exact chemical structure and guide theoretical predictions. As such, the aim of this work is not to exactly compare the experimental and theoretical results but rather to provide some insights into general trends on how functionalization can affect the properties of CNDs.

Conclusions

In conclusion, two CND syntheses with similar size but different optical properties have been presented as a comparison. The major structural difference between the suc-CNDs and the E-CNDs is the presence of nitrogenous functional groups in the E-CNDs. As a result, these particles have orders of magnitude higher PL emission, and a more distinct absorption peak at around 350 nm. To better understand the absorptive optical properties of CNDs, TDDFT was performed on twelve potential CND structures. The predicted absorption results show that the π–π* transition height is inversely correlated with the disorder of the structure, while the percent of allowed transitions positively correlates with disorder. This suggests that internal functional groups can lead to disruptions in the graphitic lattice, causing somewhat weaker but broader UV–vis spectra. Finally, the density of energy levels near the Fermi energy explains the excitation-dependent PL observed in some CNDs.

Supporting Information

The Supporting Information is available free of charge at https://pubs.acs.org/doi/10.1021/acs.jpcc.9b10373.

Acknowledgments

The authors acknowledge financial support by NSF grant (no. 1832134) and NC state fund through the Joint School of Nanoscience and Nanoengineering (JSNN). This work was performed at the JSNN, a member of the Southeastern Nanotechnology Infrastructure Corridor (SENIC) and the National Nanotechnology Coordinated Infrastructure (NNCI), which is supported by the National Science Foundation (ECCS-1542174).

References

1. Xu, X.; Ray, R.; Gu, Y.; Ploehn, H. J.; Gearheart, L.; Raker, K.; Scrivens, W. A. Electrophoretic Analysis and Purification of Fluorescent Single-Walled Carbon Nanotube Fragments. *J. Am. Chem. Soc.* **2004**, *126*, 12736– 12737, DOI: 10.1021/ja040082h

2. Cao, L.Carbon Dots for Multiphoton Bioimaging. *J. Am. Chem. Soc.* **2007**, *129*, 11318– 11319, DOI: 10.1021/ja073527l

3. Bhunia, S. K.; Saha, A.; Maity, A. R.; Ray, S. C.; Jana, N. R. Carbon Nanoparticle-Based Fluorescent Bioimaging Probes. *Sci. Rep.* **2013**, *3*, 1473, DOI: 10.1038/srep01473

4. Liang, Q.; Ma, W.; Shi, Y.; Li, Z.; Yang, X. Easy Synthesis of Highly Fluorescent Carbon Quantum Dots from Gelatin and Their Luminescent Properties and Applications. *Carbon* **2013**, *60*, 421– 428, DOI: 10.1016/j.carbon.2013.04.055

5. Liu, Y.; Xiao, N.; Gong, N.; Wang, H.; Shi, X.; Gu, W.; Ye, L. One-Step Microwave-Assisted Polyol Synthesis of Green Luminescent Carbon Dots as Optical Nanoprobes. *Carbon* **2014**, *68*, 258– 264, DOI: 10.1016/j.carbon.2013.10.086

6. Du, J.; Xu, N.; Fan, J.; Sun, W.; Peng, X. Carbon Dots for in Vivo Bioimaging and Theranostics. *Small* **2019**, *15*, 1805087, DOI: 10.1002/smll.201805087

7. Singh, R. K.; Patel, K. D.; Mahapatra, C.; Kang, M. S.; Kim, H.-W. C-Dot Generated Bioactive Organosilica Nanospheres in Theranostics: Multicolor Luminescent and Photothermal Properties Combined with Drug Delivery Capacity. *ACS Appl. Mater. Interfaces* **2016**, *8*, 24433– 24444, DOI: 10.1021/acsami.6b07494

8. Feng, T.; Ai, X.; An, G.; Yang, P.; Zhao, Y. Charge-Convertible Carbon Dots for Imaging-Guided Drug Delivery with Enhanced in Vivo Cancer Therapeutic Efficiency. *ACS Nano* **2016**, *10*, 4410– 4420, DOI: 10.1021/acsnano.6b00043

9. Hettiarachchi, S. D.; Graham, R. M.; Mintz, K. J.; Zhou, Y.; Vanni, S.; Peng, Z.; Leblanc, R. M. Triple Conjugated Carbon Dots as a Nano-Drug Delivery Model for Glioblastoma Brain Tumors. *Nanoscale* **2019**, *11*, 6192– 6205, DOI: 10.1039/c8nr08970a

10. Ji, Z.; Sheardy, A.; Zeng, Z.; Zhang, W.; Chevva, H.; Allado, K.; Yin, Z.; Wei, J. Tuning the Functional Groups on Carbon Nanodots and Antioxidant Studies. *Molecules* **2019**, *24*, 152, DOI: 10.3390/molecules24010152

11. Zeng, Z.A Fluorescence-Electrochemical Study of Carbon Nanodots (Cnds) in Bio- and Photoelectronic Applications and Energy Gap Investigation. *Phys. Chem. Chem. Phys.* **2017**, *19*, 20101– 20109, DOI: 10.1039/c7cp02875j

12. Zhang, W.; Chavez, J.; Zeng, Z.; Bloom, B.; Sheardy, A.; Ji, Z.; Yin, Z.; Waldeck, D. H.; Jia, Z.; Wei, J. Antioxidant Capacity of Nitrogen and Sulfur Codoped Carbon Nanodots. *ACS Appl. Nano Mater.* **2018**, *1*, 2699– 2708, DOI: 10.1021/acsanm.8b00404

13. Mirtchev, P.; Henderson, E. J.; Soheilnia, N.; Yip, C. M.; Ozin, G. A. Solution Phase Synthesis of Carbon Quantum Dots as Sensitizers for Nanocrystalline Tio_2 Solar Cells. *J. Mater. Chem.* **2012**, *22*, 1265– 1269, DOI: 10.1039/c1jm14112k

14. Tang, Q.; Zhu, W.; He, B.; Yang, P. Rapid Conversion from Carbohydrates to Large-Scale Carbon Quantum Dots for All-Weather Solar Cells. *ACS Nano* **2017**, *11*, 1540– 1547, DOI: 10.1021/acsnano.6b06867

15. Li, H.; Kang, Z.; Liu, Y.; Lee, S.-T. Carbon Nanodots: Synthesis, Properties and Applications. *J. Mater. Chem.* **2012**, *22*, 24230– 24253, DOI: 10.1039/c2jm34690g

16. Anwar, S.Recent Advances in Synthesis, Optical Properties, and Biomedical Applications of Carbon Dots. *ACS Appl. Bio Mater.* **2019**, *2*, 2317– 2338, DOI: 10.1021/acsabm.9b00112

17. Arcudi, F.; Đorđević, L.; Prato, M. Design, Synthesis, and Functionalization Strategies of Tailored Carbon Nanodots. *Acc. Chem. Res.* **2019**, *52*, 2070– 2079, DOI: 10.1021/acs.accounts.9b00249

18. Zhu, S.; Song, Y.; Zhao, X.; Shao, J.; Zhang, J.; Yang, B. The Photoluminescence Mechanism in Carbon Dots (Graphene Quantum Dots, Carbon Nanodots, and Polymer Dots)-Current State and Future Perspective. *Nano Res.* **2015**, *8*, 355– 381, DOI: 10.1007/s12274-014-0644-3

19. Anilkumar, P.; Wang, X.; Cao, L.; Sahu, S.; Liu, J.-H.; Wang, P.; Korch, K.; Tackett, K. N., II; Parenzan, A.; Sun, Y.-P. Toward Quantitatively Fluorescent Carbon-Based ″Quantum″ Dots. *Nanoscale* **2011**, *3*, 2023– 2027, DOI: 10.1039/c0nr00962h

20. Sun, Y.-P.; Wang, X.; Lu, F.; Cao, L.; Meziania, M. J.; Luo, P. G.; Gu, L.; Veca, L. M. Doped Carbon Nanoparticles as a New Platform for Highly Photoluminescent Dots. *J. Phys. Chem. C* **2008**, *112*, 18925– 18928, DOI: 10.1021/jp8076485

21. Deng, J.; Lu, Q.; Mi, N.; Li, H.; Liu, M.; Xu, M.; Tan, L.; Xie, Q.; Zhang, Y.; Yao, S. Electrochemical Synthesis of Carbon Nanodots Directly from Alcohols. *Chem.—Eur. J* **2014**, *20*, 4993– 4999, DOI: 10.1002/chem.201304869

22. Hu, Q.; Paau, M. C.; Zhang, Y.; Chan, W.; Gong, X.; Zhang, L.; Choi, M. M. F. Capillary Electrophoretic Study of Amine/Carboxylic Acid-Functionalized Carbon Nanodots. *J. Chromatogr. A* **2013**, *1304*, 234– 240, DOI: 10.1016/j.chroma.2013.07.035

23. Kalytchuk, S.; Poláková, K.; Wang, Y.; Froning, J. P.; Cepe, K.; Rogach, A. L.; Zbořil, R. Carbon Dot Nanothermometry: Intracellular Photoluminescence Lifetime Thermal Sensing. *ACS Nano* **2017**, *11*, 1432– 1442, DOI: 10.1021/acsnano.6b06670

24. Meiling, T. T.; Schürmann, R.; Vogel, S.; Ebel, K.; Nicolas, C.; Milosavljević, A. R.; Bald, I. Photophysics and Chemistry of Nitrogen-Doped Carbon Nanodots with High Photoluminescence Quantum Yield. *J. Phys. Chem. C* **2018**, *122*, 10217– 10230, DOI: 10.1021/acs.jpcc.8b00748

25. Strauss, V.Carbon Nanodots: Toward a Comprehensive Understanding of Their Photoluminescence. *J. Am. Chem. Soc.* **2014**, *136*, 17308– 17316, DOI: 10.1021/ja510183c

26. Li, Y.; Zhang, X.; Zheng, M.; Liu, S.; Xie, Z. Dopamine Carbon Nanodots as Effective Photothermal Agents for Cancer Therapy. *RSC Adv.* **2016**, *6*, 54087– 54091, DOI: 10.1039/c6ra02932a

27. Wang, X.; Cao, L.; Lu, F.; Meziani, M. J.; Li, H.; Qi, G.; Zhou, B.; Harruff, B. A.; Kermarrec, F.; Sun, Y.-P. Photoinduced Electron Transfers with Carbon Dots. *Chem. Commun.* **2009**, 3774– 3776, DOI: 10.1039/b906252a

28. Li, Y.; Zhao, Y.; Cheng, H.; Hu, Y.; Shi, G.; Dai, L.; Qu, L. Nitrogen-Doped Graphene Quantum Dots with Oxygen-Rich Functional Groups. *J. Am. Chem. Soc.* **2012**, *134*, 15– 18, DOI: 10.1021/ja206030c

29. Dong, Y.; Pang, H.; Yang, H. B.; Guo, C.; Shao, J.; Chi, Y.; Li, C. M.; Yu, T. Carbon-Based Dots Co-Doped with Nitrogen and Sulfur for High Quantum Yield and Excitation-Independent Emission. *Angew. Chem., Int. Ed.* **2013**, *52*, 7800– 7804, DOI: 10.1002/anie.201301114

30. Li, S.; Li, Y.; Cao, J.; Zhu, J.; Fan, L.; Li, X. Sulfur-Doped Graphene Quantum Dots as a Novel Fluorescent Probe for Highly Selective and Sensitive Detection of Fe(3+). *Anal. Chem.* **2014**, *86*, 10201– 10207, DOI: 10.1021/ac503183y

31. Omer, K. M.; Tofiq, D. I.; Hassan, A. Q. Solvothermal Synthesis of Phosphorus and Nitrogen Doped Carbon Quantum Dots as a Fluorescent Probe for Iron(Iii). *Microchim. Acta* **2018**, *185*, 466, DOI: 10.1007/s00604-018-3002-4

32. Jin, S. H.; Kim, D. H.; Jun, G. H.; Hong, S. H.; Jeon, S. Tuning the Photoluminescence of Graphene Quantum Dots through the Charge Transfer Effect of Functional Groups. *ACS Nano* **2013**, *7*, 1239– 1245, DOI: 10.1021/nn304675g

33. Casida, M. E.; Jamorski, C.; Casida, K. C.; Salahub, D. R. Molecular Excitation Energies to High-Lying Bound States from Time-Dependent Density-Functional Response Theory: Characterization and Correction of the Time-Dependent Local Density Approximation Ionization Threshold. *J. Chem. Phys.* **1998**, *108*, 4439– 4449, DOI: 10.1063/1.475855

34. Gonze, X. A Brief Introduction to the Abinit Software Package. *Z. Kristallogr.—Cryst. Mater.* **2005**, *220*, 558, DOI: 10.1524/zkri.220.5.558.65066

35. Gonze, X.Abinit: First-Principles Approach to Material and Nanosystem Properties. *Comput. Phys. Commun.* **2009**, *180*, 2582– 2615, DOI: 10.1016/j.cpc.2009.07.007

36. Gonze, X.First-Principles Computation of Material Properties: The Abinit Software Project. *Comput. Mater. Sci.* **2002**, *25*, 478– 492, DOI: 10.1016/s0927-0256(02)00325-7

37. Gonze, X.Recent Developments in the Abinit Software Package. *Comput. Phys. Commun.* **2016**, *205*, 106– 131, DOI: 10.1016/j.cpc.2016.04.003

38. Cuesta, A.; Dhamelincourt, P.; Laureyns, J.; Martínez-Alonso, A.; Tascón, J. M. D. Comparative Performance of X-Ray Diffraction and Raman Microprobe Techniques for the Study of Carbon Materials. *J. Mater. Chem.* **1998**, *8*, 2875– 2879, DOI: 10.1039/a805841e

39. Kumar, S.; Ojha, A. K.; Ahmed, B.; Kumar, A.; Das, J.; Materny, A. Tunable (Violet to Green) Emission by High-Yield Graphene Quantum Dots and Exploiting Its Unique

Properties Towards Sun-Light-Driven Photocatalysis and Supercapacitor Electrode Materials. *Mater. Today Commun.* **2017**, *11*, 76– 86, DOI: 10.1016/j.mtcomm.2017.02.009

40. Merlen, A.; Buijnsters, J.; Pardanaud, C. A Guide to and Review of the Use of Multiwavelength Raman Spectroscopy for Characterizing Defective Aromatic Carbon Solids: From Graphene to Amorphous Carbons. *Coatings* **2017**, *7*, 153, DOI: 10.3390/coatings7100153

41. Sk, M. A.; Ananthanarayanan, A.; Huang, L.; Lim, K. H.; Chen, P. Revealing the Tunable Photoluminescence Properties of Graphene Quantum Dots. *J. Mater. Chem. C* **2014**, *2*, 6954– 6960, DOI: 10.1039/c4tc01191k

42. Geethalakshmi, K. R.; Ng, T. Y.; Crespo-Otero, R. Tunable Optical Properties of Oh-Functionalised Graphene Quantum Dots. *J. Mater. Chem. C* **2016**, *4*, 8429– 8438, DOI: 10.1039/c6tc02785g

43. Li, F.; Liu, C.; Yang, J.; Wang, Z.; Liu, W.; Tian, F. Mg/N Double Doping Strategy to Fabricate Extremely High Luminescent Carbon Dots for Bioimaging. *RSC Adv.* **2014**, *4*, 3201– 3205, DOI: 10.1039/c3ra43826k

44. Fu, M.; Ehrat, F.; Wang, Y.; Milowska, K. Z.; Reckmeier, C.; Rogach, A. L.; Stolarczyk, J. K.; Urban, A. S.; Feldmann, J. Carbon Dots: A Unique Fluorescent Cocktail of Polycyclic Aromatic Hydrocarbons. *Nano Lett.* **2015**, *15*, 6030– 6035, DOI: 10.1021/acs.nanolett.5b02215

45. Xu, X.; Liu, C.; Sun, Z.; Cao, T.; Zhang, Z.; Wang, E.; Liu, Z.; Liu, K. Interfacial Engineering in Graphene Bandgap. *Chem. Soc. Rev.* **2018**, *47*, 3059– 3099, DOI: 10.1039/c7cs00836h